Dalton Transactions

ROYAL SOCIETY OF CHEMISTRY

PAPER

View Article Online
View Journal | View Issue

Cite this: *Dalton Trans.*, 2025, **54**, 12902

Preparation of multi-element soluted metal oxynitrides with a perovskite structure using precursors synthesized through a liquid-phase process

Tom Matsunaga, [a] Naoki Tarutani, [a] Kiyofumi Katagiri, *[a] Kei Inumaru, [a] Takuya Sakata,[b] Zi Lang Goo,[c] Kunihisa Sugimoto[c] and Sayako Inoué [d]

The synthesis of perovskite-type oxynitride solid solutions has gained significant attention because of their potential applications in advanced materials. This study presents a novel synthetic strategy for obtaining these solid solutions by integrating multiple elements at both the *A* and *B* sites within a single crystalline phase. Utilizing liquid-phase processes—specifically sol–gel and polymerizable complex methods—amorphous metal oxide precursors that enhance the nitridation efficiency during ammonolysis are successfully created. The incorporation of alkaline earth metals and lanthanides result in stable, single-phase perovskite structures, such as $Ca_{0.2}Sr_{0.2}Ba_{0.2}La_{0.2}Pr_{0.2}Ta(O,N)_3$, despite substantial differences in the ionic radii of the cations. Effective charge compensation through optimal ratios of O^{2-} and N^{3-} ions is achieved, enabling greater compositional flexibility. The exploration of *B*-site multi-element perovskite oxynitrides reveals that amorphous precursors facilitate the formation of solid solutions, as exemplified by $SrTi_{1/3}Nb_{1/3}Ta_{1/3}(O,N)_3$, whereas crystalline precursors lead to phase separation. Remarkably, the incorporation of up to eight metal elements in complex compositions such as $Ca_{0.2}Sr_{0.2}Ba_{0.2}La_{0.2}Pr_{0.2}Ti_{1/3}Nb_{1/3}Ta_{1/3}(O,N)_3$ and $Ca_{1/3}Sr_{1/3}Ba_{1/3}Ti_{0.2}Zr_{0.2}Hf_{0.2}Nb_{0.2}Ta_{0.2}(O,N)_3$ is demonstrated. These findings underscore the importance of precursor preparation methods in achieving the desired structural properties and pave the way for the further exploration of perovskite oxynitrides with diverse elemental combinations, thereby enhancing their functionality in various applications.

Received 22nd June 2025,
Accepted 2nd August 2025

DOI: 10.1039/d5dt01464f

rsc.li/dalton

Introduction

The synthesis of solid solutions has emerged as an essential approach for exploring the functionalities of inorganic solid materials, particularly in alloys and ceramics.[1–3] By facilitating the incorporation of diverse elements into a singular crystalline matrix, solid solutions enable the precise tuning of both the physical and chemical properties. This versatility permits the modulation of characteristics such as the electrical conductivity,[4,5] dielectric properties,[6,7] thermal conductivity,[8,9] thermal stability,[10,11] mechanical strength,[12,13] and optical behavior,[14] thereby significantly expanding the potential applications of these materials.

In recent years, the field of alloys has seen growing interest in high-entropy alloys (HEAs), which represent a contemporary trend in materials science.[15–17] HEAs are distinguished by the intentional incorporation of five or more metal elements in nearly equimolar ratios, resulting in exceptional mechanical properties and resistance to wear and corrosion. Notably, the CrMnFeCoNi alloy, commonly referred to as the Cantor alloy, has been extensively studied for its outstanding low-temperature ductility, reaching approximately 71% at room temperature.[18,19] Kitagawa *et al.* developed HEA nanoparticles containing a homogeneous atomic-level mixture of all six platinum-group elements, demonstrating exceptional catalytic activity in ethanol oxidation, surpassing conventional metal catalysts in both activity and durability.[20]

Furthermore, the concept of high entropy has recently expanded into ceramics, leading to significant research into high-entropy oxides (HEOs).[21–23] The first entropy-stabilized HEO, (Co,Cu,Mg,Ni,Zn)O, was synthesized in 2015 and exhibited a stable rock salt structure, underscoring the potential of

[a]*Graduate School of Advanced Science and Engineering, Hiroshima University, 1-4-1 Kagamiyama, Higashi-Hiroshima 739-8527, Japan. E-mail: kktgr@hiroshima-u.ac.jp*
[b]*Western Region Industrial Research Center, Hiroshima Prefectural Technology Research Institute, 2-10-1 Aga-Minami, Kure 737-0004, Japan*
[c]*Department of Chemistry, Faculty of Science and Engineering, Kindai University, 3-4-1 Kowakae, Higashi-Osaka 577-8502, Japan*
[d]*Geodynamics Research Center, Ehime University, Matsuyama 790-8577, Japan*

these materials.[24] Although HEOs have emerged only in the past decade, reported examples display a plethora of intriguing functional properties, including colossal dielectric constants,[25] low thermal conductivity,[26] and high ionic conductivity.[27] Known crystalline types of HEOs include spinel,[28,29] fluorite,[30] bixbyite,[31] and perovskite structures.[32,33] In 2018, Jiang *et al.* first reported the formation of HEOs with perovskite structures, considering 13 different compositions with Ba and Sr as *A*-site metal elements, and a combination of five elements from the Ce, Gd, Hf, Mn, Sn, Y, and Zr groups as *B*-site metal elements.[32] In this case, because alkaline earth metals that act as divalent (+2) cations are chosen as *A*-site metals, the average positive charge of the *B*-site cations must be +4 to satisfy charge compensation in the ABO_3-type structure, unless there are vacancies in the oxide anion sites. Consequently, in perovskite-type HEOs, achieving a crystal devoid of anion vacancies necessitates fixing the anion charge at −6, thereby limiting the flexibility in selecting *A*- and *B*-site elements.

To enhance the degrees of freedom in cation selection, it is essential to adjust the anionic charge within the ABO_3-type perovskite structure. Herein, we focus on the concept of mixed-anion compounds.[34,35] Most conventional ceramics consist of metallic elements in diverse combinations, yet the anions are typically restricted to a single type, mainly oxide anions (O^{2-}). However, by combining oxide ions with nitride ions (N^{3-}), which possess a different charge of −3, the compositional flexibility can be significantly improved. For example, the formation of a solid solution of $LaTaON_2$ and $SrTiO_3$, both possessing a perovskite-type structure, allows the total anion charge to vary between −6 and −8, enabling various combinations of Sr^{2+} and La^{3+} at the *A*-site, along with Ti^{4+} and Ta^{5+} at the *B*-site.[36] This flexibility facilitates precise tuning of the bandgap, thereby enhancing performance as a photocatalyst for water splitting, as previously reported.[37,38] Additional examples include the fabrication of $LaTaON_2$ and $CaTaO_2N$ solid solutions as environmentally benign inorganic pigments, which are recognized as perovskite-type metal oxynitride solid solutions.[39] However, previous studies have primarily described solid solutions with a maximum of three elements at the *A* site of perovskite-type oxynitrides ($AB(O,N)_3$),[40] and there are few examples of $AB(O,N)_3$-type solid solutions containing four or more elements at a single cation site (*A* or *B* site), or five or more elements when considering both *A* and *B* sites.

Therefore, this study aimed to establish a synthetic strategy for obtaining perovskite-type oxynitride solid solutions by mixing multiple elements into a single crystalline phase. The formation of stable solid solutions necessitates the uniform dispersion of multiple elements, which is particularly challenging in the synthesis of metal oxynitrides owing to the inherent differences in the nitridation behavior of various metals. We consider the homogeneous mixing of metal elements in the precursor to be essential for successful synthesis. Therefore, we employed liquid-phase processes, such as the sol–gel and polymerizable complex (PC) methods,[41] to synthesize precursors for the successful preparation of $AB(O,N)_3$-type solid solutions incorporating four or more cations at either the *A* or *B* site, or more than eight cations across both sites.

Experimental procedure

Materials

Titanium(IV) isopropoxide ($Ti(O\text{–}iC_3H_7)_4$, ≥99%), calcium nitrate tetrahydrate ($Ca(NO_3)_3{\cdot}4H_2O$, ≥98.5%), zirconium oxynitrate dihydrate ($ZrO(NO_3)_2{\cdot}2H_2O$, ≥99%), calcium carbonate ($CaCO_3$, ≥99.5%), strontium carbonate ($SrCO_3$, ≥98%), and titanium(IV) oxide (TiO_2, ≥99.5%) were purchased from Kishida Chemical Co., Ltd (Osaka, Japan). Strontium nitrate ($Sr(NO_3)_2$, ≥98.0%), barium nitrate ($Ba(NO_3)_2$, ≥99.0%), and niobium(V) oxide (Nb_2O_5, ≥99.9%) were obtained from FUJIFILM Wako Pure Chemical Co. (Osaka, Japan). Lanthanum nitrate hexahydrate ($La(NO_3)_3{\cdot}6H_2O$, ≥99.9%), ethylene glycol (EG, ≥99.0%), citric acid (CA, ≥99.0%), and ethanol (EtOH, ≥99.5%) were purchased from Nacalai Tesque, Inc. (Kyoto, Japan). Tantalum(V) ethoxide ($Ta(OC_2H_5)_5$, 99.9%) was supplied by Hokko Chemical Industry Co., Ltd (Tokyo, Japan). A zirconium(IV) butoxide 1-butanol solution ($Zr(O\text{–}nC_4H_9)_4$, 80% w/w), hafnium(IV) butoxide ($Hf(O\text{–}nC_4H_9)_4$, 99%), hafnium(IV) chloride ($HfCl_4$, 98%), and barium carbonate ($BaCO_3$, 99%) were obtained from Sigma-Aldrich Co., LLC (St Louis MO, USA). Praseodymium(III) nitrate hexahydrate ($Pr(NO_3)_3{\cdot}6H_2O$, ≥99.9%) was supplied by Junsei Chemical Co., Ltd (Tokyo, Japan). All reagents were used as received, without further purification. Deionized (D.I.) water used in the experiments was generated using a Millipore Milli-Q system (Merck Millipore, Billerica, MA, USA).

Preparation of *A*-site multi-element perovskite oxynitrides ($ATa(O,N)_3$; *A*: Ca, Sr, Ba, La, Pr) by the PC method

The PC method was employed to prepare mixed metal–oxide amorphous gels as precursors for *A*-site multi-element perovskite oxynitrides. Metal nitrates—$Ca(NO_3)_2{\cdot}4H_2O$, $Sr(NO_3)_2$, $Ba(NO_3)_2$, $La(NO_3)_3{\cdot}6H_2O$, and $Pr(NO_3)_3{\cdot}6H_2O$—and $Ta(OC_2H_5)_5$ were used as the starting metal sources. CA and PG served as the chelating and esterification reagents, respectively. The molar ratio of the $Ta(OC_2H_5)_5$/metal nitrate to CA/EG was maintained at 1 : 1 : 15 : 60. The metal nitrates were mixed in equimolar proportions. Initially, $Ta(OC_2H_5)_5$ and the metal nitrates were dissolved in EG, followed by the addition of CA. The solution was then heated to 150 °C to promote polymerization between CA and EG. As the reaction progressed, the solution gradually became more viscous, forming a glassy resin without visible precipitation after 1 d. The resultant resin was heat-treated to remove residual solvents and decompose unnecessary organic matter, yielding a PC-derived precursor. Solid powders of metal carbonates mixed in a mortar were prepared as precursors for comparison. $CaCO_3$, $SrCO_3$, and $BaCO_3$ powders (1 mmol in total) were mixed in a mortar with the Ta_2O_5 gel (1 mmol) obtained *via* the sol–gel method. The nitridation of the two types of precursors was performed to prepare

*A*Ta(O,N)$_3$ under a mixed gas stream of NH_3 (99.999%, 300 mL min^{-1}) and N_2 (99.99%, 300 mL min^{-1}) at 1000 °C for 3 h using a tubular furnace.

Preparation of *B*-site multi-element perovskite oxynitrides (Sr*B*(O,N)$_3$; *B*: Ti, Zr, Hf, Nb, Ta) by the PC method

B-site multi-element perovskite oxynitrides were prepared using precursors synthesized by two liquid-phase processes: the PC and sol–gel methods. The PC method was performed similarly to that used for *A*-site multi-element perovskite oxynitrides. Specifically, $ZrO(NO_3)_2{\cdot}2H_2O$, $HfCl_4$, and Ti(O–iC_3H_7)$_4$ were added to EG with continuous stirring at 150 °C until a transparent solution was obtained. Then, Nb$(OC_2H_5)_5$, Ta$(OC_2H_5)_5$, $Sr(NO_3)_2$, and CA were added to the solution and stirred at room temperature until completely dissolved. The resulting solution was subsequently heated to promote esterification between CA and EG, causing gelation, and was then heated in air to remove the solvent and unnecessary organic matter, yielding the PC-derived precursor. The nitridation of the precursor thus obtained was performed to prepare Sr*B*(O,N)$_3$ in the same manner as for *A*Ta(O,N)$_3$.

Preparation of *B*-site multi-element perovskite oxynitrides (Sr*B*(O,N)$_3$; *B*: Ti, Zr, Hf, Nb, Ta) by the sol–gel method

To prepare the precursors using the sol–gel method, amorphous oxide gels containing a homogeneous mixture of *B*-site metal elements were synthesized. A total of 1.0–2.0 mmol of metal alkoxides—Ti(O–iC_3H_7)$_4$, Zr(O–nC_4H_9)$_4$, Hf(O–nC_4H_9)$_4$, Nb$(OC_2H_5)_5$, and Ta$(OC_2H_5)_5$—were added to EtOH (5 mL). D.I. water (25 mL) was then added to the solution and vigorously mixed using a vortex mixer for 5 min. The resulting gels were collected by centrifugation, washed three times with D.I. water, and dried in an oven at 50 °C overnight. A gel containing 1 mmol of the metal compounds was then mixed with 1 mmol of $SrCO_3$ to obtain a sol–gel-derived precursor. Here, it was assumed that all the metal alkoxides used contributed to the formation of oxide gels and that no monomeric and/or oligomeric species remained in the liquid phase. Therefore, when a gel was prepared with 1 mmol of metal alkoxide, the resulting gel was treated as containing 1 mmol of metal element. Similarly, when a gel was prepared with 2 mmol, half of the resulting gel was used and treated as containing 1 mmol of metal compound. For comparison, oxide gels of the *B*-site metals were prepared separately and mixed with the Sr source in solid powder form to obtain the precursors. TiO_2, Nb_2O_5, and Ta_2O_5 gels were synthesized *via* the sol–gel method using the corresponding metal alkoxides. Each gel (total 1 mmol) was weighed and combined with 1 mmol of $SrCO_3$ in a mortar. These mixtures are referred to as comparison precursors. Nitridation of the two types of precursors thus obtained was performed to prepare Sr*B*(O,N)$_3$ in the same manner as for *A*Ta(O,N)$_3$.

Preparation of perovskite oxynitrides incorporating multiple elements at both the *A* and *B* sites

Perovskite oxynitrides with multiple elements at both the *A* and *B* sites were synthesized using amorphous metal oxides prepared *via* the PC method as precursors. The procedures for preparation of precursors and nitridation were same as for *A*Ta(O,N)$_3$ and Sr*B*(O,N)$_3$. Three types of *AB*(O,N)$_3$ samples containing eight or more metal elements were prepared: "*A* = Ca/Sr/Ba/La/Pr; *B* = Ti/Nb/Ta", "*A* = Ca/Sr/Ba; *B* = Ti/Zr/Hf/Nb/Ta", and "*A* = Ca/Sr/Ba/La/Pr; *B* = Ti/Zr/Hf/Nb/Ta".

Characterizations

Powder X-ray diffraction (XRD) was used to identify the crystalline structures of the obtained samples. Basic XRD measurements were performed using a D2 Phaser diffractometer (Bruker AXS, Karlsruhe, Germany) with Cu Kα radiation. The XRD measurement of *A*Ta(O,N)$_3$ (*A* = Ca/Sr/Ba/La/Pr) prepared using a PC-derived precursor was performed at the BL02B2 beamline of the SPring-8 synchrotron facility (Hyogo, Japan) using a wavelength of λ = 0.35429 Å. Rietveld fitting of the XRD patterns was performed using RIETAN-2000 software.

Thermogravimetric and differential thermal analyses (TG-DTA) were conducted using a TG-DTA2000S instrument (Mac Science, Co., Ltd, Tokyo, Japan). Data was collected exclusively during the heating phase, with the samples heated at a linear rate of 5 °C min^{-1} under a synthetic air flow composed of 80% N_2 and 20% O_2.

The prepared samples were observed using transmission electron microscopy (TEM; JEM-2010, JEOL, Tokyo, Japan) and scanning TEM (STEM; JEM-2100F, JEOL, Tokyo, Japan) equipped with energy-dispersive X-ray spectroscopy (EDX), operated at 200 kV using carbon film-coated 300-mesh Cu grids.

Ultraviolet–visible (UV-vis) diffuse reflectance spectra (DRS) were obtained using a UV-vis spectrophotometer (V-670; JASCO, Tokyo, Japan). The absorption spectra were processed using the Kubelka–Munk function, $F(R_\infty) = (1 - R_\infty)^2/(2R_\infty)$, where R_∞ is the absolute diffuse reflectance.[42] The band gap energies (E_g) of the samples were calculated by extrapolating the processed absorption edge.

The metal–element ratios were determined using an energy-dispersive X-ray fluorescence (XRF) spectrometer (EDX-7200, SHIMADZU, Kyoto, Japan) and a wavelength-dispersive XRF spectrometer (ZSX Primus IV, Rigaku, Tokyo, Japan).

The chromatic properties of the synthesized samples were evaluated using a chromometer (CR-400, Konica Minolta, Inc., Tokyo, Japan) in accordance with the Commission Internationale de l'Éclairage 1976 colorimetric method. In this method, $L^*a^*b^*$ values quantitatively represent color as points in a three-dimensional space. The L^* value denotes lightness, ranging from 0 (black) to 100 (white), while the a^* and b^* values indicate color directions: $+a^*$ (red), $-a^*$ (green), $+b^*$ (yellow), and $-b^*$ (blue).[43] Color saturation, C, was calculated using the equation $C = [(a^*)^2 + (b^*)^2]^{1/2}$. The hue angle, $h°$, was determined using equation the equation $h° = \tan^{-1}(b^*/a^*)$.

Results and discussion

First, we investigated the conditions for obtaining the metal oxide precursors by charring the resin prepared *via* the PC

method. Fig. S1 shows the TG-DTA curves of the resin formed by polymerization of CA and EG containing metal sources Ca, Sr, and Ta, along with XRD patterns before and after heat treatment of the resin at various temperatures: 550, 650, and 750 °C. The TG curve revealed weight loss up to 100 °C, attributed to solvent evaporation. Decomposition of the organic polymer components of the resin began at approximately 300 °C and was nearly complete by approximately 500 °C. XRD measurements showed that the resin remained amorphous both before heat treatment and after thermal treatment at 550 °C—where solvent and organic matter were largely removed—with no crystallization detected, maintaining its amorphous state. No crystallization occurred when the resin was heated at 650 °C; however, crystallization was observed after heat treatment at 750 °C. Since amorphous precursors have been shown to exhibit a superior nitridation efficiency compared with that of crystalline ones in the preparation of metal oxynitrides *via* ammonolysis and urea-nitriding methods,[44,45] we chose to use the amorphous metal oxides obtained from the resin heat-treated at 550 °C as the precursors.

A-site multi-element perovskite oxynitrides (ATa(O,N)$_3$; *A*: Ca, Sr, Ba, La, and Pr) were prepared *via* ammonolysis using PC-derived precursors. Fig. 1 shows the XRD patterns and Kubelka–Munk-transformed UV-vis DRS of the ATa(O,N)$_3$ samples obtained after nitridation of the precursors for systems employing alkaline earth metals (Ca, Sr, and Ba) as the *A* site. Binary mixtures of these elements were prepared in a 1 : 1 molar ratio, and a ternary mixture containing all three elements was prepared in equimolar proportions. In addition, for the ternary mixture, a sample was prepared using a solid powder mixture as the precursor for comparison, instead of the PC-derived precursor (denoted as "solid mixture" in Fig. 1a).

For the two-element mixtures, combinations of *A* = Ca/Sr and Sr/Ba successfully formed single-phase perovskite structures, specifically $Ca_{0.5}Sr_{0.5}TaO_2N$ and $Sr_{0.5}Ba_{0.5}TaO_2N$ (Fig. 1a). The steep absorption edge observed in the UV-vis DRS further supports the formation of solid solutions (Fig. 1b). The colors of these samples are ochre and vermilion, respectively, which are consistent with those synthesized by Kim *et al.* using the flux method.[40] Conversely, the *A* = Ca/Ba mixture resulted in two distinct phases, as indicated by the diffraction peaks in the XRD pattern and two absorption edges in the UV-vis DRS. This suggests that a single-phase perovskite $Ca_{0.5}Ba_{0.5}TaO_2N$ was not formed; instead, phase separation occurred, producing a mixture of $CaTaO_2N$ and $BaTaO_2N$. The significant difference in ionic radii[49] between Ca^{2+} (1.34 Å) and Ba^{2+} (1.61 Å) likely contributes to this phase separation.

A sample with *A* = Ca/Sr/Ba, incorporating all three elements, indicated the formation of a single-phase perovskite structure, $Ca_{1/3}Sr_{1/3}Ba_{1/3}TaO_2N$, as confirmed by XRD patterns and UV-vis DRS. This result is particularly noteworthy given the pronounced difference in the ionic radii and observed phase separation between Ca and Ba when only these two elements are mixed. The lattice volumes of the samples exhibiting a single-phase perovskite structure, along with those of each end member, were calculated. When plotted against the average ionic radii of the *A*-site cations, a linear relationship was observed (Fig. S2). These results indicate that solid solutions with a single-phase perovskite structure can be formed using mixtures of alkaline earth metal cations as the *A*-site cations in ATaO$_2$N. However, to effectively combine Ca^{2+} and Ba^{2+}—which have significantly different ionic radii—it is necessary to include Sr^{2+}, which has an intermediate ionic radius, to achieve a solid solution.

To clarify the importance of using precursors synthesized *via* the PC method, $Ca_{1/3}Sr_{1/3}Ba_{1/3}TaO_2N$ was also prepared using a mixture of ACO_3 (where *A* = Ca/Sr/Ba) as the precursor. The resulting XRD pattern showed broader and more asymmetrical peaks compared with that of the PC-derived precursor, whereas the absorption edge in the UV-vis DRS exhibited a

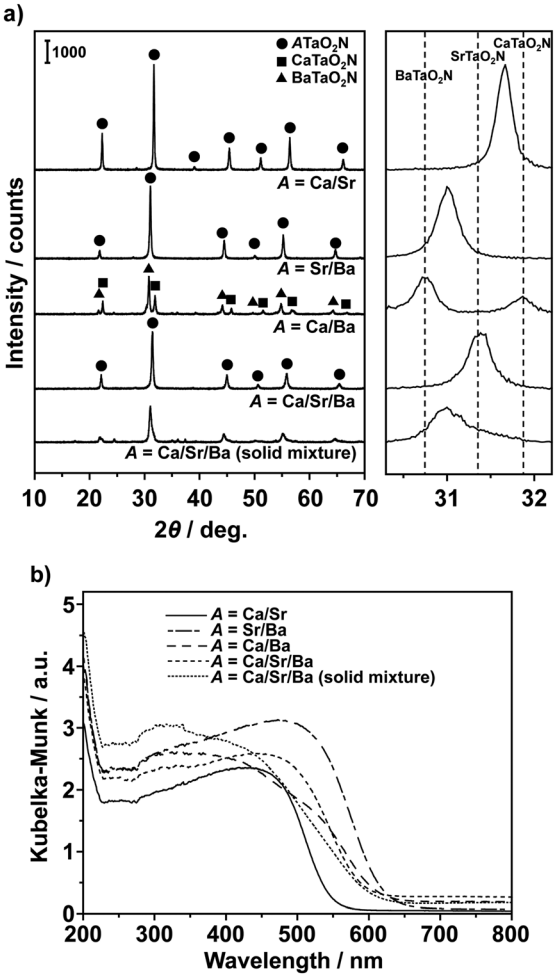

Fig. 1 (a) XRD patterns and (b) Kubelka–Munk-transformed UV-vis DRS of ATaO$_2$N (*A* = Ca/Sr, Sr/Ba, Ca/Ba, and Ca/Sr/Ba) prepared using PC-derived precursors; data for ATaO$_2$N (*A* = Ca/Sr/Ba) prepared using a solid powder mixture of ACO_3 was also shown for comparison. Enlargements of the main reflections at approximately 31° are displayed on the right of panel (a); dashed lines indicate the peak positions of $CaTaO_2N$, $SrTaO_2N$, and $BaTaO_2N$.[46]

more gradual transition. These findings suggest that the sample did not form a single-phase perovskite but instead exhibited phase separation. Kim *et al*. reported the preparation of $Ca_{1/3}Sr_{1/3}Ba_{1/3}TaO_2N$ using a mixture of solid powders as the precursor, which required the addition of KCl flux.[40] In their case, the diffusion of metal ions facilitated by the flux was crucial; however, we successfully achieved mixing of the three cations without the use of flux. This demonstrates the effectiveness of preparing the precursor *via* a liquid-phase process, which enables uniform mixing of metal ions.

Subsequently, four-(*A* = Ca/Sr/Ba/La) and five-cation mixtures (*A* = Ca/Sr/Ba/La/Pr) were prepared by introducing alkali metals and lanthanides into the *A* site of $ATa(O,N)_3$. Fig. 2 represents the XRD patterns and Kubelka–Munk-transformed UV-vis DRS of the samples obtained through the nitridation of the PC-derived precursors. Despite the presence of cations with different valences—divalent Ca^{2+}, Sr^{2+}, and Ba^{2+}, and trivalent La^{3+} and Pr^{3+}—all samples exhibited diffraction peaks corresponding to a single perovskite phase in the XRD patterns and displayed sharp absorption edge features in the UV-vis DRS (Fig. 2a and b, respectively). These results indicate that $Ca_{0.25}Sr_{0.25}Ba_{0.25}La_{0.25}Ta(O,N)_3$ and $Ca_{0.2}Sr_{0.2}Ba_{0.2}La_{0.2}Pr_{0.2}Ta(O,N)_3$ were successfully synthesized. In perovskite tantalum oxynitride $ATa(O,N)_3$, effective charge compensation can be achieved by incorporating O^{2-} and N^{3-} in an appropriate ratio, even when the average positive charge of the *A*-site cations varies between +2 and +3. This characteristic allows for greater flexibility in elemental combinations compared with multi-element perovskite metal oxides, ABO_3, where the total anion charge is fixed at −6 ($O^{2-} \times 3$).

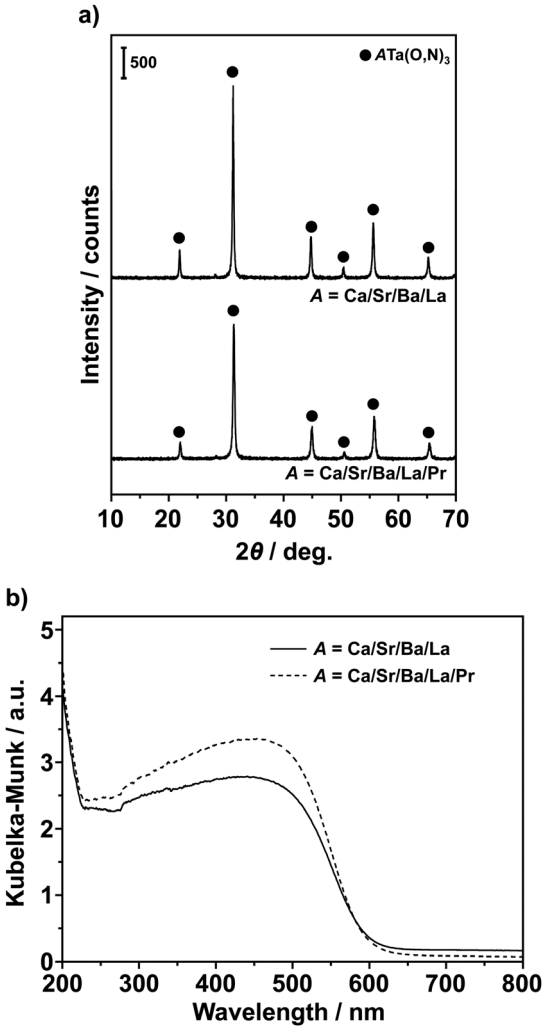

Fig. 2 (a) XRD patterns and (b) Kubelka–Munk-transformed UV-vis DRS of $ATaO_2N$ (*A* = Ca/Sr/Ba/La and Ca/Sr/Ba/La/Pr) prepared using the PC-derived precursors.

A detailed structural analysis was performed on $Ca_{0.2}Sr_{0.2}Ba_{0.2}La_{0.2}Pr_{0.2}Ta(O,N)_3$. The results of the TEM and STEM observations for $Ca_{0.2}Sr_{0.2}Ba_{0.2}La_{0.2}Pr_{0.2}Ta(O,N)_3$ are shown in Fig. 3. The high-resolution (HR) TEM image and fast Fourier transform (FFT) analysis revealed lattice spacings of 0.14, 0.16, 0.28, and 0.39 nm, corresponding to the (224), (312), (112), and (110) planes of the tetragonal perovskite structure, respectively. Elemental mapping was conducted to confirm the successful synthesis of an atomically mixed solid solution. The elemental composition was determined by STEM-EDX and XRF (Table S1). While some discrepancies in the measured values may be present owing to overlapping signals from different elements, the absence of volatile elements supports the conclusion that the molar ratios of the metal cations closely matched the intended composition. To confirm that $Ca_{0.2}Sr_{0.2}Ba_{0.2}La_{0.2}Pr_{0.2}Ta(O,N)_3$ possesses a single crystalline phase rather than a mixture of multiple crystalline phases, high-resolution synchrotron XRD analysis was conducted. Rietveld refinement was performed using the formula $Ca_{0.2}Sr_{0.2}Ba_{0.2}La_{0.2}Pr_{0.2}TaO_{1.6}N_{1.4}$ based on the elemental analysis (Fig. S3). Note that the ratio of O/N = 1.4/1.6 is not derived from actual measurements but is instead assumed based on the total charge of the cations. The resulting lattice and structural parameters are summarized in Tables S2 and S3. Among the possible space group candidates $I\bar{4}2m$, $I4/mcm$, $Fmcm$, and $Pm3m$, $I4/mcm$, which has the lowest *R*-factor, is presumed to be the most suitable space group.

Next, *B*-site multi-element perovskite oxynitrides ($SrB(O,N)_3$; *B*: Ti, Zr, Hf, Nb, and Ta) were prepared. Amorphous mixed metal oxides synthesized by a general sol–gel method using metal alkoxides for the *B*-site metal combinations were generally employed as precursors. For the five-element combination (*B* = Ti, Zr, Hf, Nb, and Ta), a precursor was prepared *via* the PC method by incorporating Sr at the *A* site. Fig. 4 illustrates the XRD patterns and Kubelka–Munk-transformed UV-vis DRS of $SrB(O,N)_3$ samples featuring combinations of two *B*-site metals (*B* = Nb/Ta, Ti/Nb, and Ti/Ta) and a three-metal combination (*B* = Ti/Nb/Ta). For comparison, data for a sample prepared using precursors containing crystalline TiO_2, Nb_2O_5, and Ta_2O_5 mixed in the solid phase are also presented. In the case of *B* = Nb/Ta, a solid solution phase, $SrNb_{0.5}Ta_{0.5}O_2N$, was successfully formed; however, for *B* = Ti/Nb and Ti/Ta, phase-separated perovskites were obtained, as indicated by the XRD patterns. Upon calculating the lattice constants for the main

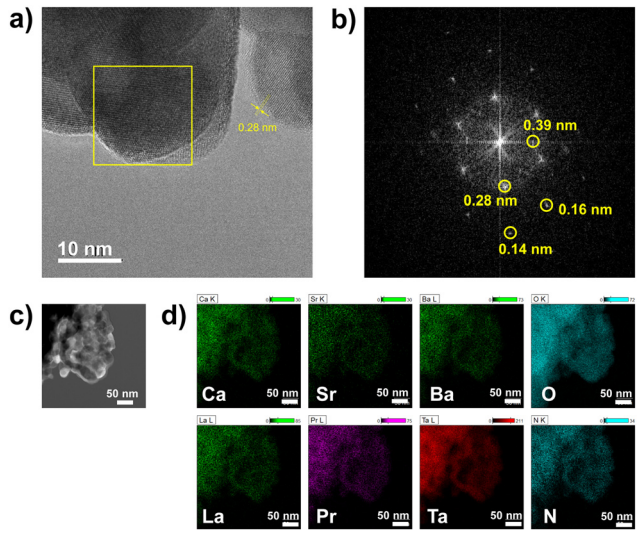

Fig. 3 (a) HRTEM and (c) high-angle annular dark field (HAADF)-STEM images and (d) elemental mappings of $Ca_{0.2}Sr_{0.2}Ba_{0.2}La_{0.2}Pr_{0.2}Ta(O,N)_3$, and (b) fast Fourier transform (FFT) of the area enclosed by the square in panel (a).

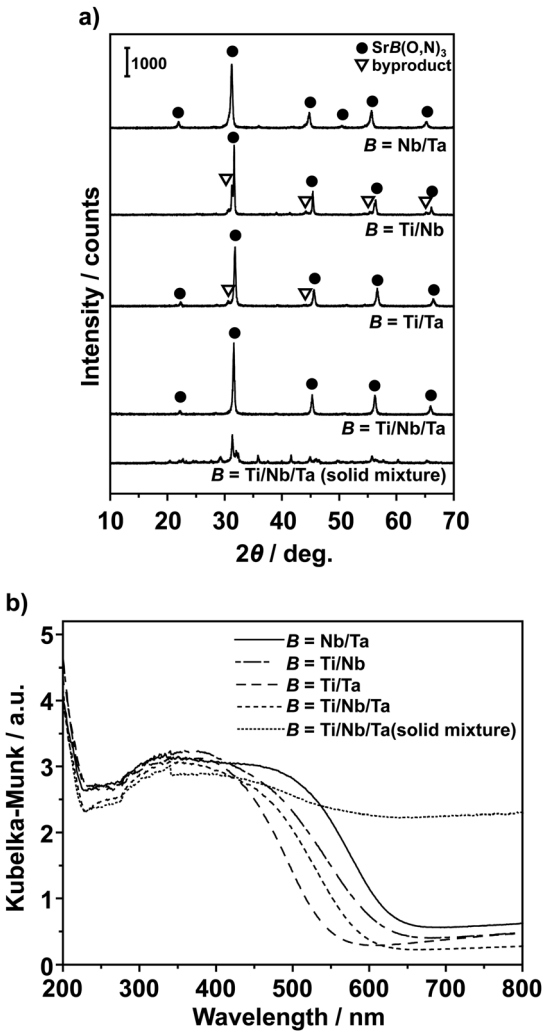

Fig. 4 (a) XRD patterns and (b) Kubelka–Munk-transformed UV-vis DRS of $SrBO_2N$ (*B* = Nb/Ta, Ti/Nb, Ti/Ta, and Ti/Nb/Ta) prepared using sol–gel-derived precursors; data for $SrBO_2N$ (B = Ti/Nb/Ta) prepared from a solid powder mixture of crystalline TiO_2, Nb_2O_5, and Ta_2O_5 is also shown for comparison.

phase of the sample with *B* = Ti/Nb from the XRD patterns, the values of a = 5.6530(5) Å and c = 8.025(8) Å were obtained. These values lie between those of $SrNbO_2N$ (a = 5.665 Å, c = 8.179 Å) and $SrTiO_3$ (a = 5.534 Å, c = 7.826 Å),[47] indicating that a solid solution of $Sr(Ti,Nb)(O,N)_3$ is partially formed. Conversely, the position of the main peak for the impurity phase at 31.2° is relatively close to the main peak of $SrNbO_2N$ at 31.3°,[48] suggesting phase separation involving $SrNbO_2N$. Similarly, for the sample with *B* = Ti/Ta, a partial solid solution of $Sr(Ti,Ta)(O,N)_3$ is present; however, achieving a complete solid solution at a 1 : 1 composition proved to be impossible. This finding is consistent with our previous report on $SrTaO_2N$–$SrTiO_3$ solid solutions, where a Ti/Ta ratio of 0.15 was identified as the upper limit.[45] The ionic radii of six-coordinated Nb^{5+} and Ta^{5+} are both 0.64 Å,[49] suggesting no significant difference and thus no barrier to solid-solution formation. Conversely, the ionic radius of six-coordinated Ti^{4+} is 0.605 Å, which is considerably smaller than those of Nb^{5+} and Ta^{5+}, which likely contributes to the observed phase separation. In contrast, a solid-solution phase, $SrTi_{1/3}Nb_{1/3}Ta_{1/3}(O,N)_3$, was effectively obtained using the three-element combination *B* = Ti/Nb/Ta. This improvement was attributed to the decrease in the Ti^{4+} ratio—from 1/2 to 1/3—since Ti^{4+} has a different ionic radius from Nb^{5+} and Ta^{5+}. No sample exhibiting a single-phase perovskite structure was obtained when a mixture of crystalline metal oxide powders was used as the precursor. This result parallels the observations for multi-element *A*-site compositions, even when multiple metal elements occupy the *B* site, successful solid-solution formation relies on preparing amorphous precursors that uniformly incorporate multiple elements at the atomic scale *via* a liquid-phase process.

The XRD patterns and UV-vis DRS results for samples containing four (*B* = Ti/Zr/Nb/Ta) and five (*B* = Ti/Zr/Hf/Nb/Ta) *B*-site metals are represented in Fig. 5. The XRD patterns indicate that all samples exhibited diffraction peaks characteristic of single-phase perovskite structures, confirming the formation of $SrTi_{0.25}Zr_{0.25}Nb_{0.25}Ta_{0.25}(O,N)_3$ and $SrTi_{0.2}Zr_{0.2}Hf_{0.2}Nb_{0.2}Ta_{0.2}(O,N)_3$ (Fig. 5a). In contrast, examination of the absorption edge *via* UV-vis DRS indicated that the sample prepared using a precursor with *B*-site metals mixed by the sol–gel method displayed a gradual absorption edge (Fig. 5b). The pronounced absorption on the longer-wavelength side suggests the presence of reducible metal ions due to the strong reducing effect of high-temperature NH_3 gas, implying incorporation of reduced species within the sample. For example, similar absorption in the longer-wavelength region was observed in the UV-vis DRS of $LaTiO_2N$, $SrNbO_2N$, and $BaTaO_2N$ synthesized by ammonolysis, which were attributed to reduced species of Ti, Nb, and Ta (such as Ti^{3+}, Nb^{4+},

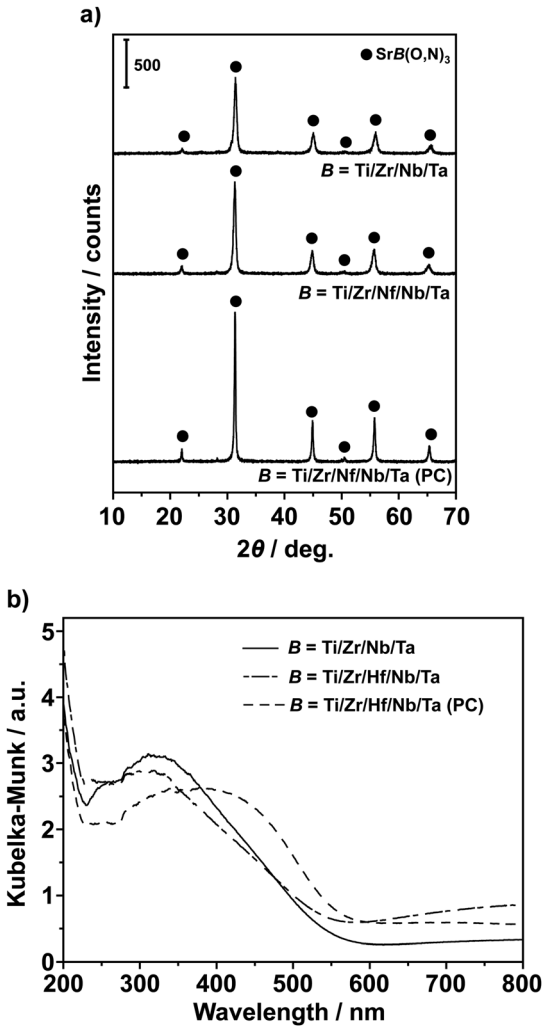

Fig. 5 (a) XRD patterns and (b) Kubelka–Munk-transformed UV-vis DRS of SrB(O,N)$_3$ (B = Ti/Zr/Nb/Ta and Ti/Zr/Hf/Nb/Ta) prepared using sol–gel-derived precursors; data for SrB(O,N)$_3$ (B = Ti/Zr/Hf/Nb/Ta) prepared using the PC-derived precursor is also provided.

Ta^{4+}) as determined by X-ray photoelectron spectroscopy, *etc.*[50–53] It is reasonable to assume that Ti^{4+}, Nb^{5+}, and Ta^{5+} are also reduced in the samples studied here. Notably, the sample synthesized using the PC-derived precursor comprising five B-site metal elements (B = Ti/Zr/Hf/Nb/Ta) and one A-site metal element (Sr) demonstrated sharper diffraction peaks in the XRD pattern and steeper absorption edges in the UV-vis DRS compared with the sample derived from the sol–gel precursor, despite identical target compositions. This disparity can be attributed to potential heterogeneities in the sol–gel-derived precursors, which are likely due to variations in the hydrolysis and condensation reaction rates of the alkoxides of the five metals during preparation. Furthermore, it is important to note that the sol–gel-derived precursor contained only B-site metals mixed in advance, whereas the PC method-derived precursor incorporated the A-site metal Sr.

Fig. 6 and 7 present TEM and STEM images of $SrTi_{0.2}Zr_{0.2}Hf_{0.2}Nb_{0.2}Ta_{0.2}(O,N)_3$ synthesized using sol–gel- and PC-derived precursors, respectively. The HRTEM images, along with the FFT analyses, reveal lattice spacings of 0.14, 0.16, 0.18, 0.20, 0.28, and 0.39 nm, corresponding to the (224), (312), (222), (220), (112), and (110) planes of the tetragonal perovskite structure, respectively. The elemental mappings shown in Fig. 6d and 7d indicate that the eight constituent elements are homogeneously distributed at the atomic level, with no detectable compositional irregularities. No significant differences were observed between the samples prepared using the two precursor methods. The elemental composition was determined using STEM-EDX and XRF techniques (Tables S4 and S5). As with previous results, no significant differences were observed in the compositions of the samples regardless of the precursor preparation method or elemental analysis technique used. This confirms that the molar ratios of the metal cations effectively retain the intended composition even when the B site consists of multiple elements, similar to the case with multi-element A-site systems. Although the XRD and UV-vis DRS results suggest that the PC-derived precursor may lead to superior properties, $SrTi_{0.2}Zr_{0.2}Hf_{0.2}Nb_{0.2}Ta_{0.2}(O,N)_3$ synthesized using the sol–gel-derived precursor also demonstrates sufficient uniformity.

Fig. 8 presents photographs of the ATa(O,N)$_3$ and SrB(O,N)$_3$ samples, which were successfully synthesized as single-phase, multi-element, mixed perovskite-type oxynitrides. The Commission Internationale de l'Éclairage $L^*a^*b^*Ch°$ color coordinates are summarized in Tables S6 and S7, along with the bandgap energies (E_g) estimated from the UV-vis DRS. The color of ATa(O,N)$_3$ transitions from yellow to orange and eventually to brown, with hue angles ($h°$) ranging from 40° to 80°. In systems containing three or more elements, the hue angles were within the range of 55° to 60°. Conversely, the color of SrB(O,N)$_3$ shifted towards green as the elements

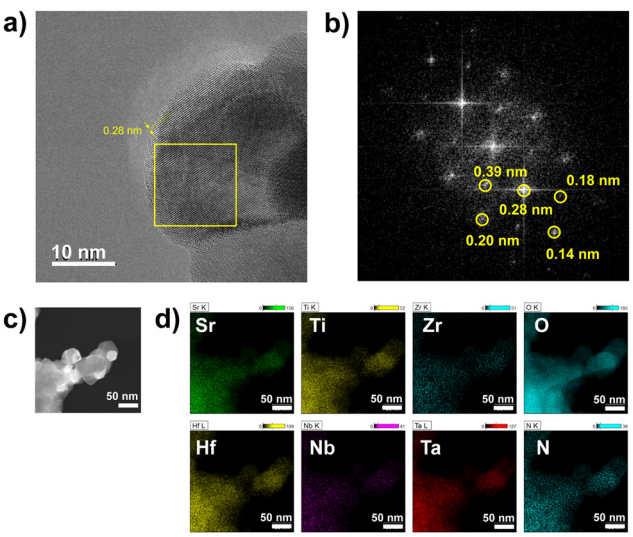

Fig. 6 (a) HRTEM and (c) HAADF-STEM images and (d) elemental mappings of $SrTi_{0.2}Zr_{0.2}Hf_{0.2}Nb_{0.2}Ta_{0.2}(O,N)_3$ prepared using the sol–gel-derived precursor, and (b) FFT of the area enclosed by the square in panel (a).

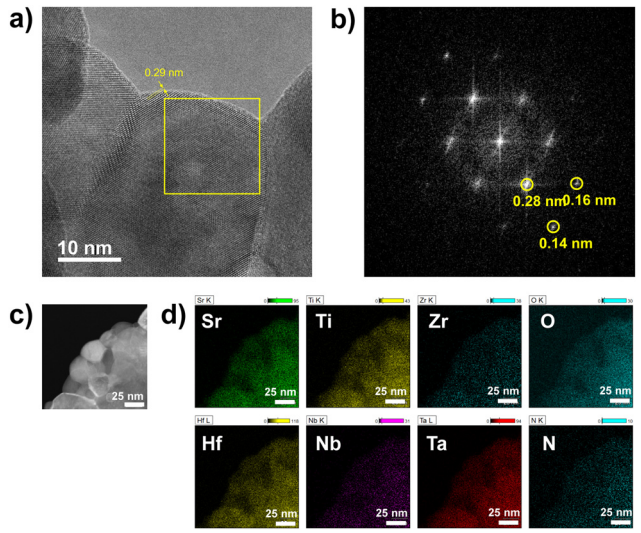

Fig. 7 (a) HRTEM and (c) HAADF-STEM images and (d) elemental mappings of $SrTi_{0.2}Zr_{0.2}Hf_{0.2}Nb_{0.2}Ta_{0.2}(O,N)_3$ prepared using the PC-derived precursor, and (b) FFT of the area enclosed by the square in panel (a).

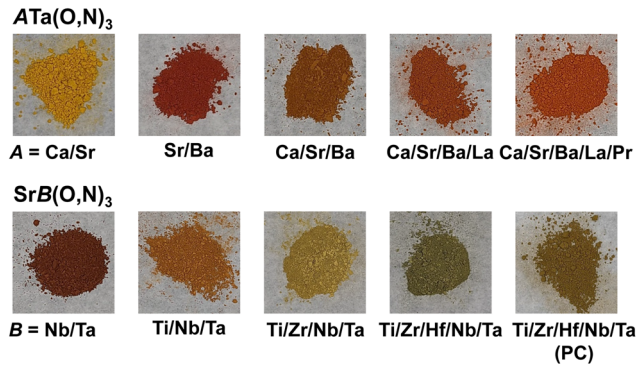

Fig. 8 Photographic images of $ATa(O,N)_3$ (A = Ca/Sr, Sr/Ba, Ca/Sr/Ba, Ca/Sr/Ba/La, and Ca/Sr/Ba/La/Pr) prepared using PC-derived precursors, and $SrB(O,N)_3$ (B = Nb/Ta. Ti/Nb/Ta, Ti/Zr/Nb/Ta, and Ti/Zr/Hf/Nb/Ta) prepared using sol–gel-derived precursors. An image of $SrB(O,N)_3$ (B = Ti/Zr/Hf/Nb/Ta) synthesized using a PC-derived precursor is also included.

were mixed, resulting in an elevated hue angle. Notably, $SrTi_{0.2}Zr_{0.2}Hf_{0.2}Nb_{0.2}Ta_{0.2}(O,N)_3$ exhibited a hue angle of approximately 100°, the highest among the synthesized samples. The UV-vis DRS of the sample with green color shows an increased background absorption in the longer-wavelength region, as seen in Fig. 5b, suggesting a reduction of B site cations, *i.e.*, Nb^{5+} to Nb^{4+} and Ti^{4+} to Ti^{3+}. The mixed of absorption from these reduced species with band gap absorption resulting in the green color has also been reported in previous syntheses of $LaTiO_2N$.[50] Furthermore, the E_g values exhibited relatively minor variations compared with the pronounced color changes, remaining in the range of approximately 2.0 to 2.3 eV. These findings suggest that the strategic combination of multiple elements at both the A and B sites can significant alter the color of perovskite-type oxynitrides. This characteristic highlights their potential application not only as visible light-responsive photocatalysts but also as inorganic pigments for coloring purposes.

Finally, perovskite oxynitrides incorporating multiple elements at both the A and B sites were synthesized. The precursors used were amorphous metal oxides containing all relevant metal elements, prepared *via* the PC method. Fig. 9 shows the XRD patterns of three $AB(O,N)_3$ samples: "A = Ca/Sr/Ba/La/Pr; B = Ti/Nb/Ta", "A = Ca/Sr/Ba; B = Ti/Zr/Hf/Nb/Ta", and "A = Ca/Sr/Ba/La/Pr; B = Ti/Zr/Hf/Nb/Ta". In the sample containing a mixture of ten elements—specifically, "A = Ca/Sr/Ba/La/Pr; B = Ti/Zr/Hf/Nb/Ta"—peaks not attributable to the perovskite structure were observed and identified as by-products. These peaks correspond closely to the diffraction pattern of $A_2B_2O_7$ (A = La and/or Pr; B = Zr and/or Hf), characterized by a pyrochlore structure,[54–56] indicating the formation of pyrochlore-type oxides as mixed phases or solid solutions. It has been reported that synthesizing $LaZrO_2N$, which contains La at the A site and Zr at the B site, is more challenging than producing other $AB(O,N)_3$-type oxynitrides. The formation of $LaZrO_2N$ competes with the generation of pyrochlore-type oxides, necessitating prolonged ammonolysis treatment.[57] Consequently, the simultaneous inclusion of La and/or Pr at the A site and Zr and/or Hf at the B site may facilitate the production of oxides other than oxynitrides. To address this, samples were synthesized by combining eight metal elements, excluding La and Pr from the A-site elements and Zr and Hf from the B-site elements—specifically, "A = Ca/Sr/Ba/La/Pr; B = Ti/Nb/Ta" and "A = Ca/Sr/Ba; B = Ti/Zr/Hf/Nb/Ta". In these cases, the diffraction peaks corresponding to the perovskite-type structure manifested as a single phase, confirming the successful formation of solid solutions containing these elements: $Ca_{0.2}Sr_{0.2}Ba_{0.2}La_{0.2}Pr_{0.2}Ti_{1/3}Nb_{1/3}Ta_{1/3}(O,N)_3$ and

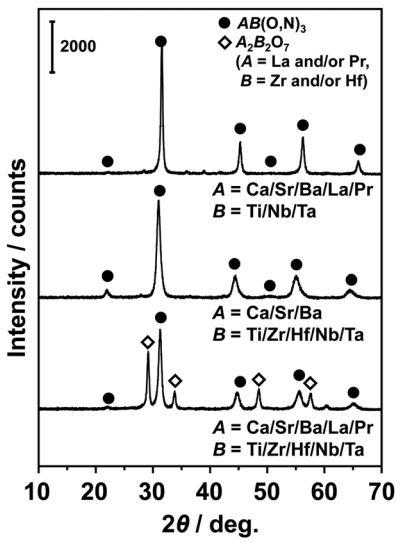

Fig. 9 XRD patterns of $AB(O,N)_3$ ("A = Ca/Sr/Ba/La/Pr; B = Ti/Nb/Ta", "A = Ca/Sr/Ba; B = Ti/Zr/Hf/Nb/Ta", and "A = Ca/Sr/Ba/La/Pr; B = Ti/Zr/Hf/Nb/Ta") prepared using PC-derived precursors.

Table 1 Elemental compositions of $Ca_{0.2}Sr_{0.2}Ba_{0.2}La_{0.2}Pr_{0.2}Ti_{1/3}Nb_{1/3}Ta_{1/3}(O,N)_3$ and $Ca_{1/3}Sr_{1/3}Ba_{1/3}Ti_{0.2}Zr_{0.2}Hf_{0.2}Nb_{0.2}Ta_{0.2}(O,N)_3$ determined by the wavelength-dispersive XRF

	Ca	Sr	Ba	La	Pr	Ti	Zr	Hf	Nb	Ta	O	N
$Ca_{0.2}Sr_{0.2}Ba_{0.2}La_{0.2}Pr_{0.2}Ti_{1/3}Nb_{1/3}Ta_{1/3}(O,N)_3$	2.56 (0.19)	5.86 (0.20)	8.79 (0.19)	8.32 (0.18)	11.0 (0.23)	5.53 (0.34)	— (—)	— (—)	11.2 (0.35)	19.6 (0.31)	17.8 (1.87)	9.47 (1.13)
$Ca_{1/3}Sr_{1/3}Ba_{1/3}Ti_{0.2}Zr_{0.2}Hf_{0.2}Nb_{0.2}Ta_{0.2}(O,N)_3$	4.64 (0.33)	10.7 (0.34)	16.1 (0.33)	— (—)	— (—)	3.54 (0.21)	5.75 (0.18)	12.3 (0.19)	7.23 (0.19)	13.2 (0.20)	23.4 (2.61)	3.10 (0.39)

The values in the upper row indicates wt%, and the values in parentheses in the lower row indicate the molar ratios of the *A* site, *B* site, and anion site, each of which sums to 1, 1, and 3, respectively.

$Ca_{1/3}Sr_{1/3}Ba_{1/3}Ti_{0.2}Zr_{0.2}Hf_{0.2}Nb_{0.2}Ta_{0.2}(O,N)_3$. The results of the quantitative analysis of all 10 elements, including cations and anions, for these two types of perovskite-type oxynitrides containing these eight metal elements are summarized in Table 1, using wavelength-dispersive XRF. In addition to the measured wt%, considering that the general formula for perovskite oxynitrides is $AB(O,N)_3$, the molar ratios are presented in parentheses, ensuring that the total for the cation at the *A* site and the cation at the *B* site is 1 each, while the total for the anion sites O and N is 3. For $Ca_{0.2}Sr_{0.2}Ba_{0.2}La_{0.2}Pr_{0.2}Ti_{1/3}Nb_{1/3}Ta_{1/3}(O,N)_3$, it can be seen that the five elements at the *A* site are *ca.* 20% each, according to the intended ratio, while the three elements at the *B* site are *ca.* 33% each. Based on these measured values, the total charge at the cation and anion sites in the formula $AB(O,N)_3$ is about +7.1 and −7.1, respectively, indicating that charge balance is maintained. Similarly, for $Ca_{1/3}Sr_{1/3}Ba_{1/3}Ti_{0.2}Zr_{0.2}Hf_{0.2}Nb_{0.2}Ta_{0.2}(O,N)_3$, it can be seen that the three elements at the *A* site are *ca.* 33% each, while the five elements at the *B* site are *ca.* 20% each. Based on these measured values, the total charge at the cation and anion sites in the formula $AB(O,N)_3$ is about +6.4 and −6.4, respectively, also indicating that charge balance is maintained. These results demonstrate that even when multiple cations with different valences are mixed at the *A* and *B* sites, the ratio of O to N at the anion site can be freely adjusted to maintain the charge balance between cations and anions in the perovskite structure. To the best of our knowledge, no perovskite-type oxynitrides containing these eight metal elements within a single-crystal structure have been synthesized to date, representing the largest combination of elements achieved in a multi-element mixed perovskite-type oxynitride. The key to this achievement was the synthesis of amorphous metal oxides, in which metal elements were uniformly mixed *via* a liquid-phase method and subsequently used as precursors.

Conclusions

In this study, we successfully prepared a diverse array of perovskite oxynitrides featuring multiple elements at both the *A* and *B* sites, utilizing amorphous metal oxide precursors derived from liquid-phase processes, including the sol–gel and PC methods. Maintaining an amorphous state was critical, as it improved the nitridation efficiency during ammonolysis compared with crystalline precursors. The incorporation of alkaline earth metals and lanthanides at the *A* sites resulted in the formation of single-phase perovskite structures. Notably, we successfully synthesized solid solutions such as $Ca_{0.2}Sr_{0.2}Ba_{0.2}La_{0.2}Pr_{0.2}Ta(O,N)_3$ despite significant differences in the ionic radii of the cations. The ability to achieve effective charge compensation through optimized ratios of O^{2-} and N^{3-} ions further enhanced flexibility in elemental combinations. In addition, our exploration of *B*-site multi-element perovskite oxynitrides demonstrated that the use of amorphous precursors facilitated the formation of solid solutions, as exemplified by $SrTi_{1/3}Nb_{1/3}Ta_{1/3}(O,N)_3$, whereas the use of

crystalline precursors led to phase separation. This finding underscored the importance of precursor preparation methods for achieving the desired structural properties. Remarkably, we successfully incorporated eight metal elements at both *A* and *B* sites, yielding complex compositions such as $Ca_{0.2}Sr_{0.2}Ba_{0.2}La_{0.2}Pr_{0.2}Ti_{1/3}Nb_{1/3}Ta_{1/3}(O,N)_3$ and $Ca_{1/3}Sr_{1/3}Ba_{1/3}Ti_{0.2}Zr_{0.2}Hf_{0.2}Nb_{0.2}Ta_{0.2}(O,N)_3$. Overall, our findings highlight the critical role of precursor preparation methods in controlling the phase behavior and structural properties, paving the way for the exploration of perovskite oxynitrides that integrate a wide variety of elements, thereby enhancing their potential applications in advanced materials science.

Author contributions

TM: investigation, writing – original draft; NT: investigation, methodology, writing –review & editing; KK: conceptualization, funding acquisition, methodology, supervision, writing – review & editing; KI: supervision; TS: investigation & resources; ZLG: investigation; KS: resources; SI: investigation & resources.

Conflicts of interest

The authors declare no conflicts of interest.

Data availability

Raw data were generated at Hiroshima University. The data that support the findings of this study are available from the corresponding author, KK, upon reasonable request.

Supplementary information is available: TG-DTA curves and XRD patterns of the precursors, comparison of the average of *A*-site ion radius and the lattice volume of the sample, elemental compositions, Rietveld-refined XRD pattern, lattice parameters, structure parameters, CIE color coordinates and bandgap energies. See DOI: **https://doi.org/10.1039/d5dt01464f**.

Acknowledgements

This work was supported by JSPS KAKENHI Grant Numbers JP22H05142, JP22H05143, JP22H05145, JP23H00236, JP24K21810, and JP25K01859. TM was supported by JST SPRING Grant Number JPMJSP2132. The synchrotron radiation experiments were performed at the BL02B2 of SPring-8 with the approval of the Japan Synchrotron Radiation Research Institute (JASRI) (Proposal No. 2024A1551). We also acknowledge Dr Hiroshi Fukuoka (Hiroshima University) for his assistance with the Rietveld analysis and calculation of lattice constants. We would like to thank Editage (**https://www.editage.jp**) for English language editing.

References

1 W. D. Callister Jr. and D. G. Rethwisch, *Materials Science and Engineering: An Introduction*, Wiley, Hoboken, NJ, USA, 10th edn, 2020.
2 A. G. Khachaturyan, *Prog. Mater. Sci.*, 1978, **22**, 1–150.
3 M. Lusi, *Cryst. Growth Des.*, 2018, **18**, 3704–3712.
4 K. Sasaki, H. P. Seifert and L. J. Gauckler, *J. Electrochem. Soc.*, 1994, **141**, 2759–2768.
5 K. Maki, Y. Ito, H. Matsunaga and H. Mori, *Scr. Mater.*, 2013, **68**, 777–780.
6 A. A. Heitmann and G. A. Rossetti Jr., *J. Am. Ceram. Soc.*, 2014, **97**, 1661–1685.
7 D. Y. Lu, X. C. Li, M. Toda, X. F. Wang and X. Y. Sun, *J. Ceram. Soc. Jpn.*, 2009, **117**, 828–831.
8 W. D. Kingery, *J. Am. Ceram. Soc.*, 1959, **42**, 617–627.
9 G. P. Meisner, D. T. Morelli, S. Hu, J. Yang and C. Uher, *Phys. Rev. Lett.*, 1998, **80**, 3551–3554.
10 M. Ishitsuka, T. Sato, T. Endo and M. Shimada, *J. Am. Ceram. Soc.*, 1987, **70**, 69–71.
11 S. Mohammadkhani, E. Schaal, A. Dolatabadi, C. Moreau, B. Davis, D. Guay and L. Roué, *J. Am. Ceram. Soc.*, 2019, **102**, 5063–5070.
12 N. P. Allen, T. H. Schofield and A. E. L. Tate, *Nature*, 1951, **168**, 378–379.
13 L. Gao, R. S. Chen and E. H. Han, *J. Alloys Compd.*, 2009, **481**, 379–384.
14 H. Ji, Z. Huang, Z. Xia, M. S. Molokeev, V. V. Atuchin, M. Fang and Y. Liu, *J. Phys. Chem. C*, 2015, **119**, 2038–2045.
15 J. W. Yeh, S. K. Chen, S. J. Lin, J. Y. Gan, T. S. Chin, T. T. Shun, C. H. Tsau and S. Y. Chang, *Adv. Eng. Mater.*, 2004, **6**, 299–303.
16 D. B. Miracle and O. N. Senkov, *Acta Mater.*, 2017, **122**, 448–511.
17 E. P. George, D. Raabe and R. O. Ritchie, *Nat. Rev. Mater.*, 2019, **4**, 515–534.
18 B. Cantor, I. T. H. Chang, P. Knight and A. J. B. Vincent, *Mater. Sci. Eng., A*, 2004, **375–377**, 213–218.
19 B. Cantor, *Prog. Mater. Sci.*, 2021, **120**, 100754.
20 D. Wu, K. Kusada, T. Yamamoto, T. Toriyama, S. Matsumura, S. Kawaguchi, Y. Kubota and H. Kitagawa, *J. Am. Chem. Soc.*, 2020, **142**, 13833–13838.
21 A. Sarkar, O. Wang, A. Schiele, M. R. Chellali, S. S. Bhattacharya, D. Wang, T. Brezesinski, H. Hahn, L. Velasco and B. Breitung, *Adv. Mater.*, 2019, **31**, 1806236.
22 C. Oses, C. Toher and S. Curtarolo, *Nat. Rev. Mater.*, 2020, **5**, 295–309.
23 R. Z. Zhang and M. J. Reece, *J. Mater. Chem. A*, 2019, **7**, 22148–22162.
24 C. M. Rost, E. Sachet, T. Borman, A. Moballegh, E. C. Dickey, D. Hou, J. L. Jones, S. Curtarolo and J. P. Maria, *Nat. Commun.*, 2015, **6**, 8485.
25 D. Bérardan, S. Franger, D. Dragoe, A. K. Meena and N. Dragoe, *Phys. Status Solidi RRL*, 2016, **10**, 328–333.
26 Y. Zhang, M. Xie, Z. Wang, X. Song, R. Mu, J. Gao, J. Bao, F. Zhou and W. Pan, *J. Alloys Compd.*, 2023, **958**, 170471.

27 D. Bérardan, S. Franger, A. K. Meena and N. Dragoe, *J. Mater. Chem. A*, 2016, **4**, 9536–9541.
28 A. Mao, H. Z. Xiang, Z. G. Zhang, K. Kuramoto, H. Zhang and Y. Jia, *J. Magn. Magn. Mater.*, 2020, **497**, 165884.
29 Z. Grzesik, G. Smoła, M. Miszczak, M. Stygar, J. Dąbrowa, M. Zajusz, K. Świerczek and M. Danielewski, *J. Eur. Ceram. Soc.*, 2020, **40**, 835–839.
30 J. Gild, M. Samiee, J. L. Braun, T. Harrington, H. Vega, P. E. Hopkins, K. Vecchio and J. Luo, *J. Eur. Ceram. Soc.*, 2018, **38**, 3578–3584.
31 R. Djenadic, A. Sarkar, O. Clemens, C. Loho, M. Botros, V. S. K. Chakravadhanula, C. Kübel, S. S. Bhattacharya, A. S. Gandhi and H. Hahn, *Mater. Res. Lett.*, 2016, **5**, 102–109.
32 S. Jiang, T. Hu, J. Gild, N. Zhou, J. Nie, M. Qin, T. Harrington, K. Vecchio and J. Luo, *Scr. Mater.*, 2018, **142**, 116–120.
33 A. Sarkar, R. Djenadic, D. Wang, C. Hein, R. Kautenburger, O. Clemens and H. Hahn, *J. Eur. Ceram. Soc.*, 2018, **38**, 2318–2327.
34 H. Kageyama, K. Hayashi, K. Maeda, J. P. Attfield, Z. Hiroi, J. M. Rondinelli and K. R. Poeppelmeier, *Nat. Commun.*, 2018, **9**, 772.
35 K. Maeda, F. Takeiri, G. Kobayashi, S. Matsuishi, H. Ogino, S. Ida, T. Mori, Y. Uchimoto, S. Tanabe, T. Hasegawa, N. Imanaka and H. Kageyama, *Bull. Chem. Soc. Jpn.*, 2022, **95**, 26–37.
36 H. Kato, K. Ueda, M. Kobayashi and M. Kakihana, *J. Mater. Chem. A*, 2015, **3**, 11824–11829.
37 K. Maeda and K. Domen, *Angew. Chem., Int. Ed.*, 2012, **51**, 9865–9869.
38 C. Pan, T. Takata, M. Nakabayashi, T. Matsumoto, N. Shibata, Y. Ikuhara and K. Domen, *Angew. Chem., Int. Ed.*, 2015, **54**, 2955–2959.
39 M. Jansen and H. P. Letschert, *Nature*, 2000, **404**, 980–982.
40 J. W. Seol, Y. I. Kim, T. L. Pham and J. S. Lee, *J. Korean Ceram. Soc.*, 2020, **57**, 432–439.
41 M. Kakihana, M. Arima, Y. Nakamura, M. Yashima and M. Yoshimura, *Chem. Mater.*, 1999, **11**, 438–450.
42 P. Kubelka and F. Munk, *Z. Tech. Phys.*, 1931, **12**, 593–601.
43 R. M. Johnston, in *Pigment Handbook*, ed. T. C. Putton, Wiley-Interscience, New York, 1973, vol. 3, pp. 229–288.
44 S. Yamamoto, Y. Ohashi, Y. Masubuchi, T. Takeda, T. Motohashi and S. Kikkawa, *J. Alloys Compd.*, 2009, **482**, 160–163.
45 T. Sakata, R. Yoshiyuki, S. Urushidani, N. Tarutani, K. Katagiri and K. Inumaru, *J. Sol-Gel Sci. Technol.*, 2022, **104**, 685–693.
46 S. Balaz, S. H. Porter, P. M. Woodward and L. J. Brillson, *Chem. Mater.*, 2013, **25**, 3337–3343.
47 N. Umezawa and A. Janotti, *ChemSusChem*, 2016, **9**, 1027–1031.
48 K. Fujii, K. Shimada and M. Yashima, *J. Ceram. Soc. Jpn.*, 2017, **125**, 808–810.
49 R. D. Shannon, *Acta Crystallogr., Sect. A*, 1976, **32**, 751–767.
50 R. Okada, K. Katagiri, Y. Masubuchi and K. Inumaru, *Eur. J. Inorg. Chem.*, 2019, **2019**, 1257–1264.
51 K. Kawashima, M. Hojamberdiev, H. Wagata, K. Yubuta, S. Oishi and K. Teshima, *Cryst. Growth Des.*, 2015, **15**, 333–339.
52 B. Siritanaratkul, K. Maeda, T. Hisatomi and K. Domen, *ChemSusChem*, 2011, **4**, 74–78.
53 M. Higashi, R. Abe, T. Takata and K. Domen, *Chem. Mater.*, 2009, **21**, 1543–1549.
54 T. Sui, Q. Feng, N. Luo, J. He, H. Huang, C. Yuan, Z. Cen and X. Chen, *J. Mater. Chem. C*, 2024, **12**, 8426–8434.
55 F. Zhong, L. Shi, J. Zhao, G. Cai, Y. Zheng, Y. Xiao and J. Long, *Ceram. Int.*, 2017, **43**, 11799–11806.
56 M. Pokhrel, S. K. Gupta, K. Wahid and Y. Mao, *Inorg. Chem.*, 2019, **58**, 1241–1251.
57 S. J. Clarke, B. P. Guinot, C. W. Michie, M. J. C. Calmont and M. J. Rosseinsky, *Chem. Mater.*, 2002, **14**, 288–294.